REFERENCES AND NOTES

1. W. B. Hubbard and J. M. MacFarlane, *J. Geophys. Res.* **85**, 225 (1980).
2. W. B. Hubbard *et al.*, *Science* **253**, 648 (1991).
3. R. V. Eck, E. R. Lippincott, M. O. Dayhoff, Y. T. Pratt, *ibid.* **153**, 628 (1966).
4. W. J. Nellis, F. H. Ree, M. Van Thiel, A. C. Mitchell, *J. Chem. Phys.* **75**, 3055 (1981).
5. M. Ross, *Nature* **292**, 435 (1981).
6. W. G. Hoover, *Computational Statistical Mechanics* (Elsevier, Amsterdam, 1991).
7. P. Focher, G. L. Chiarotti, M. Bernasconi, E. Tosatti, M. Parrinello, *Europhys. Lett.* **26**, 345 (1994); S. Scandolo, M. Bernasconi, G. L. Chiarotti, P. Focher, E. Tosatti, *Phys. Rev. Lett.* **74**, 4015 (1995).
8. The simulation cell is allowed to vary in shape and volume, driven by the quantum mechanically calculated internal stress (*21*). The ion-electron interaction is modeled with a fully nonlocal pseudopotential for carbon and a local pseudopotential for hydrogen. Electron-electron interactions are treated within the local density approximation, with gradient corrections as described in (*22*). A plane-wave basis set with a kinetic energy cutoff of 40 rydberg has been used for the electronic wave functions, which are assumed to have the same periodicity as the (varying) simulation cell.
9. This finding is consistent with shock-wave experiments (*4*), which reveal a discontinuity in the CH_4 equation of state at 20 GPa and 2000 K.
10. The time scale of our simulations is such that a few hundred C–H stretching oscillations and a few tens of molecular collisions take place in each run. Although this is typically a sufficient time scale for thermalization, and in fact dissociation took place in a fraction of a picosecond, processes like segregation and diffusion occur on a longer time scale. These processes are energetically minor in comparison with dissociation and will not significantly alter the dissociation picture as proposed.
11. W. J. Nellis, F. H. Ree, R. J. Trainor, A. C. Mitchell, M. B. Boslough, *J. Chem. Phys.* **80**, 2789 (1984).
12. W. J. Nellis *et al.*, *Science* **240**, 779 (1988).
13. M. S. Somayazulu, L. W. Finger, R. J. Hemley, H. K. Mao, *ibid.* **271**, 1400 (1996).
14. F. H. Ree, *J. Chem. Phys.* **70**, 974 (1979).
15. Mixtures, of course, do not represent a well-defined state at $T = 0$. Their enthalpy is an upper bound to that of the true low-temperature system, where single phases are likely to prevail.
16. In spite of the endothermic character of the zero-pressure conversion $16\,CH_4 \rightarrow 2\,CH_4 + 4\,C_2H_6 + 2\,C_3H_8 + 8\,H_2$ (enthalpy of reaction $\Delta H° = 0.37$ eV per CH_4 molecule), the volume reduction ΔV brought by the 100-GPa conversion leads to a $P\Delta V$ contribution of about 0.65 eV per CH_4 molecule and to an enthalpy gain of about 0.4 eV per CH_4 molecule.
17. Moreover, a comparison of simulated vibrational spectra of the mixture and of CH_4 shows a significant broadening of the C–H bending mode band around 800 to 1700 cm^{-1} in the mixture. This fact, together with the presence of the H_2 stretching mode at 4200 cm^{-1}, should be looked for as the signature of the CH_4 dissociation in forthcoming low-temperature diamond–anvil cell experiments.
18. J. I. Moses, K. Rages, J. B. Pollack, *Icarus* **113**, 232 (1995).
19. B. Bezard, P. N. Romani, B. J. Conrath, W. C. Maguire, *J. Geophys. Res.* **96**, 18961 (1991).
20. Unsaturated molecules such as C_2H_2 do not withstand the pressure conditions of the middle ice layers (*23*).
21. P. Focher and G. L. Chiarotti, in *Progress in Computational Physics of Matter*, L. Reatto and F. Manghi, Eds. (World Scientific, Singapore, 1995), pp. 1–42.
22. A. D. Becke, *Phys. Rev. A* **38**, 3098 (1988); J. P. Perdew, *Phys. Rev. B* **33**, 8822 (1986).
23. M. Bernasconi, M. Parrinello, G. L. Chiarotti, P. Focher, E. Tosatti, in *Proceedings of the Joint XV AIRAPT & XXXIII EHPRG International Conference on High Pressure Science & Technology*, W. A. Trzeciakowski, Ed. (World Scientific, Singapore, 1996), p. 846.
24. S. Scandolo, G. L. Chiarotti, E. Tosatti, *Phys. Rev. B* **53**, 5051 (1996).
25. J. Kohanoff, G. L. Chiarotti, S. Scandolo, E. Tosatti, in preparation.
26. Results for CH_4 and hydrocarbon mixtures were obtained from low-temperature simulations. Results for diamond and hydrogen were obtained from standard total-energy calculations carried out separately, with the same level of accuracy, for carbon (*24*) and for hydrogen (*25*).

27. We acknowledge useful discussions with J. Kohanoff. The work at SISSA was partly supported by the European Commission and the Italian Research Council.

26 September 1996; accepted 23 December 1996

Burst Conditions of Explosive Volcanic Eruptions Recorded on Microbarographs

Meghan M. Morrissey* and Bernard A. Chouet

Explosive volcanic eruptions generate pressure disturbances in the atmosphere that propagate away either as acoustic or as shock waves, depending on the explosivity of the eruption. Both types of waves are recorded on microbarographs as 1- to 0.1-hertz N-shaped signals followed by a longer period coda. These waveforms can be used to estimate burst pressures and gas concentrations in explosive volcanic eruptions and provide estimates of eruption magnitudes.

Since first photographed during the 1975 eruption of Ngauruhoe Volcano in New Zealand (*1*), atmospheric shock waves and condensation clouds marking their passage in the near field of the source have become well-recognized features of explosive volcanic eruptions (*2–4*). Occurrences of shock waves were documented in video footage of the 1992 eruptions of Mount Spurr, Alaska, where the shocks were observed propagating through the column of ash in a series of flashes occurring within the plume (*4*). These flashes represent short-lived clouds produced by the propagation of shock waves through the local atmosphere, which momentarily condenses water vapor. A vigorous ejection of a mixture of hot gases and rock fragments characteristic of a vulcanian eruption followed the flashes. Air waves accompanying vulcanian eruptions are recorded on microbarographs as N-shaped signals followed by a longer period coda. Here we use numerical simulations to demonstrate how the amplitude and waveform of atmospheric pressure waves may be used to estimate both burst pressure (or preexplosion gas pressure) and gas concentration of ejecta for discrete, explosive eruptions. Recognition and analysis of such pressure signals may aid in the detection of explosive eruptions and subsequent ash plumes in remote areas.

The types of eruption signals recorded on microbarographs (Fig. 1, A to E) range from sharp N-shaped waves, such as that observed at the onset of the 1883 eruption at Krakatoa (*5*), to long-period oscillations, such as those recorded during the 15 June 1991 eruption at Mount Pinatubo (*6*). The spectral peaks associated with the latter type of disturbance have been interpreted as the characteristic periods of the acoustic and gravity modes of the atmosphere triggered by a continuous flux of thermal energy from a Plinian eruption (*7–10*). N-shaped waveforms are commonly associated with acoustic disturbances produced by discrete explosive eruptions (Fig. 1).

Within the past 25 years, a variety of numerical models have been used to estimate the burst pressures of vulcanian eruptions from observed maximum ejecta velocities (*11–15*). Early models based on the Bernoulli equation (*11, 12*) overestimated burst pressures by an order of magnitude because they neglected the compressibility of the gas phase (*13*) in the solid-gas mixture. In these and later models, the gas phase is H_2O, which makes up >90% by weight of total gas exsolved from magma situated at depths shallower than 3 to 4 km. More recent models have taken into account not only gas compressibility (*13, 14*) but also the relative motion of ejecta of variable sizes and the air through which the ejecta travel (*15*). In the most recent model (*15*), burst pressures were estimated as functions of gas concentration for a given travel distance, launch velocity, launch angle, and diameter of ejected fragments. Like the earlier models (*11–13*), this latter model was applied to the 1975 Ngauruhoe eruption, the classic example of a vulcanian eruption. Burst pressures ranging up to 10 MPa for gas concentrations of between 2 to 6 weight % H_2O were calculated for ejecta parameters measured in photographs. The accuracy of this model depends primarily on how well ejecta parameters are constrained. Here we introduce an alternative method for independently estimating the burst pressures and gas concentrations based on the wave-

M. M. Morrissey, U.S. Geological Survey, Box 25046, Federal Center, MS-966, Denver, CO 80225, USA.
B. A. Chouet, U.S. Geological Survey, 345 Middlefield Road, MS-977, Menlo Park, CA 94025, USA.

*To whom correspondence should be addressed.

forms of atmospheric disturbances produced by the Ngauruhoe eruption and other documented vulcanian events (*2*, *3*, *8*, *9*).

Most models of atmospheric response to explosive eruptions are concerned mainly with the far-field signals and use either a point-compressive source or a point-injection source with a source duration ranging up to a few minutes (*7*, *8*, *16*, *17*). Although such models are useful to estimate the magnitude of large-scale eruptions, they provide few details about the eruption. As demonstrated in (*5*), explosive eruptions generate pressure disturbances that undergo refraction and attenuation as they propagate through the atmosphere (*7*) and can excite acoustic-gravity modes at periods larger than 30 s (*8*, *16*). To extract information from the waveform regarding the physics of an eruption, it is best to study the signal closer to the source, where the waveform is simple and sharp (*18*).

Using results from numerical simulations, we demonstrate how preeruption conditions in the conduit might be manifested in the waveform of the atmospheric disturbance. Our numerical model is an adaptation of the numerical code DASH (dusty air shock), which solves the Navier-Stokes equations in cylindrical coordinates for a mixture of gas and solid particles by means of an explicit multifield finite difference representation (*19*). The governing equations consist of a system of eight coupled, nonlinear, partial differential equations, in which closure is achieved by the inclusion of the thermomechanical equations of state for the respective phases, and the heat and momentum transfer functions. DASH calculates the spatiotemporal variations of pressure, density, velocity, and internal energy in a hot, gas-solid particle mixture expanding from the exit plane of a conduit into an unconfined, cool, stratified, isothermal atmosphere (*19*, *20*). Details of the code and its applications are given in (*19–24*).

To simulate the discharge of a conduit flow into the atmosphere, a cylindrical cavity is set up at the lower boundary of the computational domain. The conduit walls are assumed to be perfectly rigid, and the appropriate boundary conditions are applied for rigid reflectors. The fluid mixture inside the conduit is initially at rest and is pressurized according to the weight of the lava dome cap (*13*). During the burst phase of the simulated eruption, which is marked by the instantaneous removal of cap rock, flow conditions at the exit plane of the conduit are choked; hence, the exit velocity is equal to the sound speed of the mixture. Choked conditions at the vent prevail until the conduit pressure decays to atmospheric pressure. The eruption terminates when the supply of fluid inside the conduit is exhausted.

In all simulations, the conduit geometry is scaled according to the parameters estimated for Sakurajima Volcano (*2*). Our model uses a mixture of steam and 1-mm-diameter particles with a density of 2350 kg/m^3. To limit the number of gas phases in the model, we have assumed that the atmosphere is steam with a sound speed of 440 m/s. The gas and particulate phases are assumed to be in thermal equilibrium (*20*) at 950°C initially, the solidus temperature of andesitic magmas commonly associated with vulcanian eruptions (*15*). In one simulation (Fig. 2, A to D), a shock wave formed instantaneously in the atmosphere at the onset of discharge. The shock wave

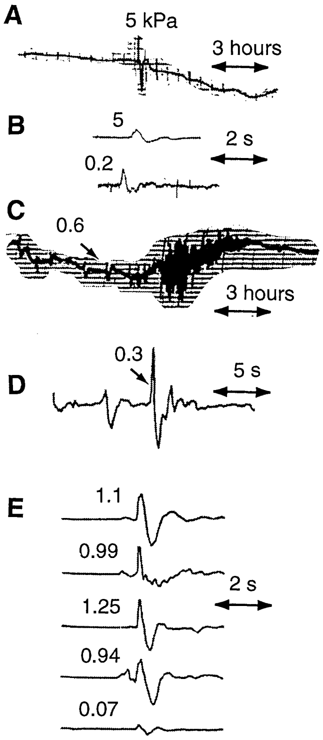

Fig. 1. Examples of microbarograms obtained for eruptions at (**A**) Mount St. Helens in 1980 at 54 km (*7*); (**B**) Sakurajima Volcano, Japan, in 1989 at 5 km (*2*); (**C**) Mount Pinatubo in 1991 at 21 km (*8*); (**D**) Ruapehu Volcano, New Zealand, in 1995 at 9 km (*9*); and (**E**) Mount Tokachi in 1988 through 1989 at 3.5 km (*3*). The locations of the microbarographs are relative to the vent. All of the onsets of the waveforms are characterized by an N-shaped pulse. The peak-to-peak pressure (in kilopascals) represents the difference between the maximum and minimum pressures of the pulse. In (C), more than nine N-shaped pulses occurred before the long-period oscillation related to the Plinian phase of the eruption, which lasted for more than 6 hours. The pulses are assumed to be related to discrete, precursory explosive events. Only 5 of the 13 pulses recorded at Mount Tokachi in 1988 through 1989 are shown; all data are included in Fig. 3C.

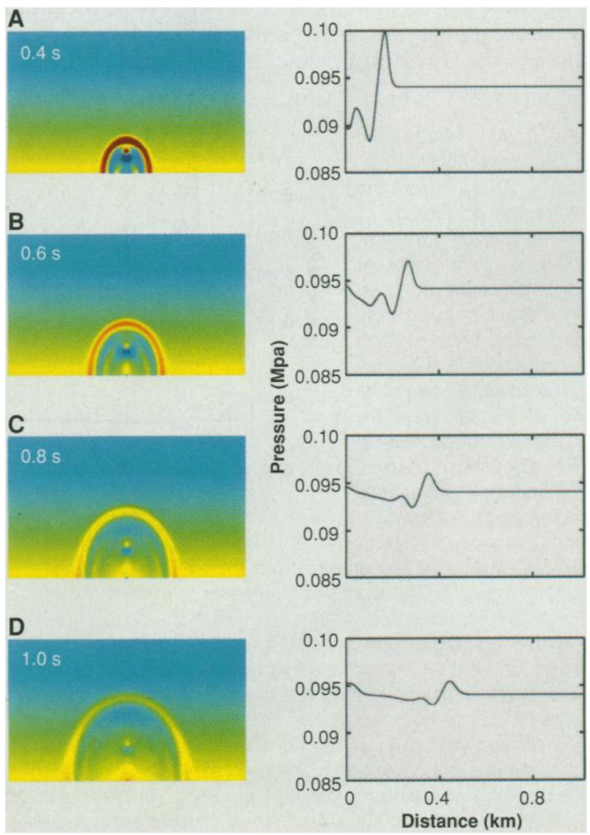

Fig. 2. (**A** to **D**) Snapshots (at left) of the pressure field in the atmosphere for a simulated eruption with a burst pressure of 5 MPa and a solid-to-gas mass ratio of 1 (50 weight % H_2O). The computational domain extends to an altitude of 1 km and a radial distance of 1 km. The color scale is proportional to the magnitude of pressure with red representing the highest pressure and blue denoting the lowest pressure. The red shell represents the shock wave formed during the initial discharge of fluid from the conduit. The blue-green and green-yellow shells inside the red shell represent the trailing expansion and compression waves, which reestablish the pressure behind the shock wave to atmospheric pressure. The red dot below the trailing compression wave represents the front of the discharging fluid. To the right of each snapshot is a horizontal pressure profile extending to a distance of 1 km from the vent axis at an altitude of 50 m. The amplitude of the N-shaped wave associated with the shock wave decreases as it travels away from the vent.

was initially coupled to the ejecta front but separated from the plume after 0.6 s when the plume reached its maximum altitude (*19*). The shock wave is characterized by a sharp increase in atmospheric pressure (Fig. 2). The pressure dropped below atmospheric pressure behind the shock front, forming an N-shaped wave. As the N wave propagated away from the vent, the peak-to-peak amplitude of the signal decayed, and a trailing compression wave developed that increased the pressure behind the shock front back to atmospheric pressure (Fig. 2, B to D).

Comparisons of four simulations with different burst pressures (Fig. 3A) show that the peak-to-peak pressure P_k of the atmospheric wave is a function of the burst pressure P_b. For example, the wave produced by an eruption with $P_b = 0.2$ MPa yielded $P_k = 0.005$ MPa at a distance of 100 m and altitude of 50 m, whereas an eruption with $P_b = 1.0$ MPa yielded $P_k = 0.015$ MPa at the same location. The relation between P_k and P_b may be used to estimate P_b from measurements of the air wave, as demonstrated in Fig. 3, B and C. The values of P_k derived from the microbarograms in Fig. 1 fall within the set of decay curves illustrated in Fig. 3C, suggesting burst pressures of 0.1 to 1 MPa for Mount Tokachi, 0.2 to 5 MPa for Sakurajima, and 0.2 to 0.5 MPa for Ruapehu. The average P_k from the 1991 Mount Pinatubo explosive events corresponds to $P_b > 5$ MPa. The value of P_k for the shock waves recorded during the 1975 Ngauruhoe eruption (*1*) corresponds to burst pressures of 5 to 6 MPa, which are within the range of the burst pressures estimated from the trajectory paths of ejected clasts (*15*). Similar data are not available for the other simulated eruptions.

The rise time of the atmospheric wave depends on the amount of H_2O in the discharging rock particles–steam mixture (Fig. 3D). The rise time for a steam-rich mixture (95 weight % H_2O) was much faster than that of a particle-rich mixture (5 weight % H_2O). This sensitivity of the waveform to gas concentration reflects the amount of energy dissipation in the plume and is also a function of the sound speed of the discharging mixture, all of which vary with the solid-to-gas mass ratio of the mixture (*20*). For the steam-rich mixture in Fig. 3D, the initial sound speed of the mixture (875 m/s) was greater than the sound speed of the atmosphere (440 m/s), and the pressure wave was a shock wave characterized by a sharp N-shaped waveform. For the particle-rich mixture in Fig. 3D, the initial sound speed of the mixture (170 m/s) was less than the sound speed of the atmosphere, and the pressure wave was an acoustic wave characterized by a weaker N-shaped waveform. As illustrated in Fig. 3E, the propagation speeds of the pressure waves related to different H_2O content either decelerate or accelerate to converge to the sound speed of the atmosphere at short distances from the vent. If the atmosphere were air, the curves would converge to 340 m/s instead of 440 m/s. Within 500 m from the vent, the waves travel at characteristic speeds that vary as functions of the H_2O content.

Although the signatures of the simulated atmospheric waves are simple in comparison to the data (Fig. 1), our results illustrate the type of information that can be extracted from various parts of the waveform. The amplitude of the impulsive onset of the waveform is indicative of the burst pressure of the mixture discharging from the vent and provides useful information for the detection of an explosive eruption and for an estimation of the eruption magnitude. The rise time of waveforms recorded on microbarographs located within 1 km of the vent can be used to constrain the gas concentration in the eruption column. Pressure sensors are inexpensive and can easily be incorporated into existing monitoring networks (*25*). In contrast, other methods to measure gas concentrations in eruption plumes such as correlation spectrometry require expensive equipment, which prevents their use in a permanent monitoring network.

The waves following the impulsive onset in many of the microbarograms in Fig. 1 are not reproduced by our simulations and may represent a combination of path effects or additional minor bursts or acoustic emissions from trapped expansion waves reverberating in the conduit as observed in laboratory and numerical experiments (*5*, *26*). Expansion waves did occur in the conduit during simulated eruptions. However, their amplitudes were quite small (<0.1 MPa) as shown in Fig. 4, A to C (the same information is shown on a magnified scale in Fig. 4, D to F).

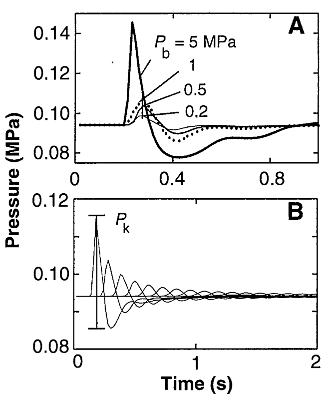

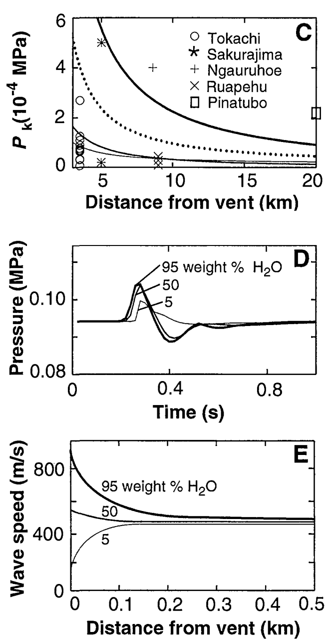

Fig. 3. (**A**) Pressure-time plots obtained at a distance of 100 m from the vent and an altitude of 50 m, derived from simulations with different burst pressures P_b given in units of megapascals and a gas concentration of 50 weight % H_2O. The peak-to-peak pressure P_k of the air wave increases with increasing P_b. (**B**) Waveforms obtained at 50-m intervals along a profile extending to a distance of 1 km from the vent at an altitude of 50 m. These waveforms are derived from the simulated eruption shown in Fig. 2. The values of P_k measured in these waveforms are fitted by a power law from which the curves in (C) are derived. (**C**) Decay curves of P_k for distances ranging up to 20 km from the vent for the four simulations shown in (A). The symbols represent the data in Fig. 1, A to E. (**D**) Pressure-time plots obtained at the same receiver location as in (A), derived from simulations with a fixed $P_b = 0.5$ MPa for different gas concentrations. The rise time of the waveform decreases with increasing gas concentration. (**E**) Wave speed of pressure disturbances obtained from simulations shown in (D) plotted along a profile extending to a distance of 500 m from the vent at an altitude of 50 m.

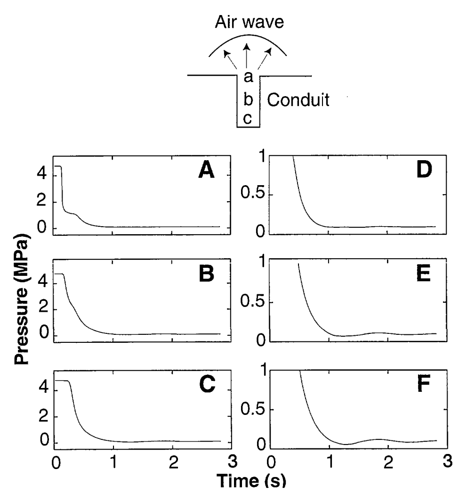

Fig. 4. (**A** to **C**) Pressure-time histories at three different depths in the conduit for the simulated eruption shown in Fig. 2. (**D** to **F**) Same pressure-time histories shown at a magnified scale to enhance the amplitude of decaying pressure oscillations associated with the trapped waves.

REFERENCES AND NOTES

1. I. A. Nairn, *Nature* **259**, 190 (1976).
2. M. Iguchi and K. Ishihara, *Annu. Dis. Prev. Res. Inst.* **33B-1**, 1 (1990).
3. H. Okada, Y. Nishimura, H. Miyamachi, H. Mori, K. Ishihara, *Bull. Volcanol. Soc. Jpn.* **35**, 175 (1990).
4. Alaska Volcano Observatory, *Eos* **74**, 221 (1993).
5. S. W. Kieffer and B. Sturtevant, *J. Geophys. Res.* **89**, 8253 (1984).
6. H. Kanamori and J. Mori, *ibid.* **87**, 5422 (1982).
7. J. R. Reed, *ibid.* **92**, 11979 (1987).
8. H. Kanamori and J. W. Given, *Geophys. Res. Lett.* **19**, 721 (1992).
9. Ruapehu Surveillance Group, *Eos* **77**, 189 (1996).
10. H. Kanamori, J. Mori, D. G. Harkrider, *J. Geophys. Res.* **99**, 21947 (1994).
11. R. F. Fudali and W. G. Melson, *Bull. Volcanol.* **35**, 383 (1972).
12. A. R. McBirney, *ibid.* **37**, 443 (1973).
13. S. Seif, L. Wilson, I. A. Nairn, *Nature* **277**, 440 (1979).
14. L. Wilson, *J. Volcanol. Geotherm. Res.* **8**, 297 (1980).
15. S. A. Fagents and L. Wilson, *Geophys. J. Int.* **113**, 359 (1993).
16. S. A. Francis, *J. Geophys. Res.* **78**, 2278 (1973).
17. M. J. Buckingham and M. A. Garces, *ibid.* **101**, 8129 (1996).
18. S. Vergniolle, G. Brandeis, J. C. Mareschal, *ibid.*, p. 20449.
19. G. A. Valentine, *Los Alamos Lab. Rep. LA-1141-T* (1988).
20. ——— and K. H. Wohletz, *J. Geophys. Res.* **94**, 1867 (1989).
21. K. H. Wohletz and G. A. Valentine, in *Magma Storage and Transport*, M. Ryan, Ed. (Wiley, New York, 1976), p. 113.
22. G. A. Valentine, K. H. Wohletz, S. W. Kieffer, *Geol. Soc. Am. Bull.* **104**, 154 (1992).
23. S. W. Kieffer and M. M. Morrissey, *Geotimes* **38**, 5 (1993).
24. M. M. Morrissey and B. A. Chouet, *J. Geophys. Res.*, in press.
25. J. A. Power *et al.*, *ibid.* **62**, 69 (1994).
26. A. W. Woods and S. M. Bower, *Earth Planet. Sci. Lett.* **131**, 189 (1995).

27. We thank D. Hill and J. Lowenstern for helpful reviews. M.M.M. is grateful to the National Science Foundation for the postdoctoral fellowship under which part of this work was carried out.

27 September 1996; accepted 11 December 1996

Deciding Advantageously Before Knowing the Advantageous Strategy

Antoine Bechara, Hanna Damasio, Daniel Tranel, Antonio R. Damasio*

Deciding advantageously in a complex situation is thought to require overt reasoning on declarative knowledge, namely, on facts pertaining to premises, options for action, and outcomes of actions that embody the pertinent previous experience. An alternative possibility was investigated: that overt reasoning is preceded by a nonconscious biasing step that uses neural systems other than those that support declarative knowledge. Normal participants and patients with prefrontal damage and decision-making defects performed a gambling task in which behavioral, psychophysiological, and self-account measures were obtained in parallel. Normals began to choose advantageously before they realized which strategy worked best, whereas prefrontal patients continued to choose disadvantageously even after they knew the correct strategy. Moreover, normals began to generate anticipatory skin conductance responses (SCRs) whenever they pondered a choice that turned out to be risky, before they knew explicitly that it was a risky choice, whereas patients never developed anticipatory SCRs, although some eventually realized which choices were risky. The results suggest that, in normal individuals, nonconscious biases guide behavior before conscious knowledge does. Without the help of such biases, overt knowledge may be insufficient to ensure advantageous behavior.

In a gambling task that simulates real-life decision-making in the way it factors uncertainty, rewards, and penalties, the players are given four decks of cards, a loan of $2000 facsimile U.S. bills, and asked to play so that they can lose the least amount of money and win the most (*1*). Turning each card carries an immediate reward ($100 in decks A and B and $50 in decks C and D). Unpredictably, however, the turning of some cards also carries a penalty (which is large in decks A and B and small in decks C and D). Playing mostly from the disadvantageous decks (A and B) leads to an overall loss. Playing from the advantageous decks (C and D) leads to an overall gain. The players have no way of predicting when a penalty will arise in a given deck, no way to calculate with precision the net gain or loss from each deck, and no knowledge of how many cards they must turn to end the game (the game is stopped after 100 card selections). After encountering a few losses, normal participants begin to generate SCRs before selecting a card from the bad decks (*2*) and also begin to avoid the decks with large losses (*1*). Patients with bilateral damage to the ventromedial prefrontal cortices do neither (*1, 2*).

A. Bechara and D. Tranel, Department of Neurology, Division of Behavioral Neurology and Cognitive Neuroscience, University of Iowa College of Medicine, Iowa City, IA 52242, USA.
H. Damasio and A. R. Damasio, Department of Neurology, Division of Behavioral Neurology and Cognitive Neuroscience, University of Iowa College of Medicine, Iowa City, IA 52242, and The Salk Institute of Biological Studies, La Jolla, CA 92186, USA.

*To whom correspondence should be addressed.

To investigate whether subjects choose correctly only after or before conceptualizing the nature of the game and reasoning over the pertinent knowledge, we continuously assessed, during their performance of the task, three lines of processing in 10 normal participants and in 6 patients (*3*) with bilateral damage of the ventromedial sector of the prefrontal cortex and decision-making defects. These included (i) behavioral performance, that is, the number of cards selected from the good decks versus the bad decks; (ii) SCRs generated before the selection of each card (*2*); and (iii) the subject's account of how they conceptualized the game and of the strategy they were using. The latter was assessed by interrupting the game briefly after each subject had made 20 card turns and had already encountered penalties, and asking the subject two questions: (i) "Tell me all you know about what is going on in this game." (ii) "Tell me how you feel about this game." The questions were repeated at 10-card intervals and the responses audiotaped.

After sampling all four decks, and before encountering any losses, subjects preferred decks A and B and did not generate significant anticipatory SCRs. We called this period pre-punishment. After encountering a few losses in decks A or B (usually by card 10), normal participants began to generate anticipatory SCRs to decks A and B. Yet by card 20, all indicated that they did not have a clue about what was going on. We called this period pre-hunch (Fig. 1). By about card 50, all normal participants began to express a "hunch" that decks A and B were riskier and all generated anticipatory SCRs whenever they pondered a choice from deck A or B. We called this period hunch. None of the patients generated anticipatory SCRs or expressed a "hunch" (Fig. 1). By card 80, many normal participants expressed knowledge about why, in the long run, decks A and B were bad and decks C and D were good. We called this period conceptual. Seven of the 10 normal participants reached the conceptual period, during which they continued to avoid the bad decks, and continued to generate SCRs whenever they considered sampling again from the bad decks. Remarkably, the three normal participants who did not reach the conceptual period still made advantageous choices (*4*). Just as remarkably, the three patients with prefrontal damage who reached the conceptual period and correctly described which were the bad and good decks chose disadvantageously. None of the patients generated anticipatory SCRs (Fig. 1). Thus, despite an accurate account of the task and of the correct strategy, these patients failed to generate au-